

Fitting Gravitational Lenses: Truth or Delusion

N. Wyn Evans^{1,2} and Hans J. Witt³

¹ *Theoretical Physics, 1 Keble Rd, Oxford, OX1 3NP*

² *Institute of Astronomy, Madingley Rd, Cambridge, CB3 0HA*

³ *Baumkamp 8, 22299 Hamburg, Germany*

10 November 2018

ABSTRACT

The observables in a strong gravitational lens are usually just the image positions and sometimes the flux ratios. We develop a new and simple algorithm which allows a set of models to be fitted exactly to the observations. Taking our cue from the strong body of evidence that early-type galaxies are close to isothermal, we assume that the lens is scale-free with a flat rotation curve. External shear can be easily included. Our algorithm allows full flexibility as regards the angular structure of the lensing potential. Importantly, all the free parameters enter linearly into the model and so *the lens and flux ratio equations can always be solved by straightforward matrix inversion*. The models are only restricted by the fact that the surface mass density must be positive.

We use this new algorithm to examine some of the claims made for anomalous flux ratios. It has been argued that such anomalies betray the presence of substantial amounts of substructure in the lensing galaxy. We demonstrate by explicit construction that some of the lens systems for which substructure has been claimed can be well-fit by smooth lens models. This is especially the case when the systematic errors in the flux ratios (caused by microlensing or differential extinction) are taken into account. However, there is certainly one system (B 1422+231) for which the existing smooth models are definitely inadequate and for which substructure may be implicated.

Within a few tens of kpc of the lensing galaxy centre, dynamical friction and tidal disruption are known to be very efficient at dissolving any substructure. Very little substructure is projected within the Einstein radius. The numbers of strong lenses for which substructure is currently being claimed may be so large that this contradicts rather than supports cold dark matter theories.

Key words: gravitational lensing – galaxies: structure – galaxies: elliptical – dark matter

1 INTRODUCTION

The fitting of models to observational data has always been a major concern in strong gravitational lensing (e.g., Schechter 2000). In most cases, the lens is only composed of 2 (a “doublet”) or 4 (a “quadruplet”) point-like images. For the doublets, the observable constraints are the four relative coordinates of the images with respect to the lensing galaxy, together with the one flux ratio of the first image to the second. For the quadruplets, this becomes eight relative coordinates and three flux ratios. Only for a handful of lens systems are time delays available. It therefore happens very frequently that lens models have more degrees of freedom than the number of constraining observations. In fact, the situation is often even worse than we have just described. Sometimes the centre of the lensing galaxy itself cannot be reliably identified. Sometimes a lens system is complicated

by the possible effects of nearby bright galaxies. Very often, the flux ratios are untrustworthy, either because of differential extinction in the optical bands (e.g., Falco et al. 1999) or because of microlensing in the optical and radio (e.g., Irwin et al. 1989; Koopmans & de Bruyn 2000) or because of scintillation, scatter-broadening and free-free absorption in the radio (e.g., Patnaik et al. 1992, Jones et al. 1996, Winn, Rusin & Kochanek 2003). It is therefore already clear that considerable caution must be exercised in interpreting the results of fits to gravitational lens systems.

The approach of modellers has been largely two-pronged. First, general non-parametric methods have been developed (e.g., Saha & Williams 1997). These have proved powerful in exploring the range of degeneracies in the lensing mass that can give rise to a particular image configuration. For example, in the case of PG 1115+080, Saha & Williams present three different models obeying the lens-

ing constraints, but for which the lensing mass distribution resembles a face-on spiral, an edge-on disk or a flattened elliptical galaxy respectively. Second, many simple parametric models have been thoroughly explored, such as those based on elliptically stratified potentials (e.g., Witt 1996; Witt & Mao 1997) or densities (e.g., Kassiola & Kovner 1993; Muñoz, Kochanek & Keeton 2001). The advantage of this is that the models may already incorporate some of the known properties of nearby galaxies. However, this approach may also be dangerous because simple ansätze like elliptical potentials or surface mass densities can introduce unexpected properties. These properties may be so severe that, for example, the flux ratios may not be well fitted and wrong conclusions may be drawn. This can be seen most clearly in the case of elliptical potentials, in which there are strong constraints on the flux ratios (e.g., Witt & Mao 2000; Hunter & Evans 2001).

All this attains added significance in the light of recent claims of evidence for substructure from “anomalous flux ratios” in strong lensing. Mao & Schneider (1998) were the first to point out that substructure may be needed to explain the flux ratios in some cases. The instance that they selected, the quadruplet B 1422+231, has three highly magnified bright images and one much fainter image. Three highly magnified images occur generically near a cusp, and a Taylor expansion gives a universal relationship that the sum of the fluxes of the two outer images should equal the flux of the middle image. This is strongly violated in B 1422+231 leaving substructure on top of the smooth model as the believable culprit. This result is supported by the detailed models of B 1422+231 by Bradac et al. (2002) which find that the discrepancy requires substructure on the mass scale $\sim 10^6 M_\odot$. Recently, Dalal & Kochanek (2002) looked at seven predominantly radio quadruplets and argued that the flux ratios were anomalous by comparison with those expected for simple isothermal lenses with external shear. They claimed that the anomalous flux ratios implied the existence of ~ 2 per cent of the mass of the lensing galaxy in substructure. Metcalf & Zhao (2002) looked at five optical quadruplets and similarly claimed evidence for anomalous flux ratios on comparison with those expected for simple elliptical power-law potentials with shear. The problem with this procedure is, of course, that anomalous flux ratios may not be the result of substructure at all, but may simply reflect deficiencies in the modelling.

This motivates us to introduce in sections 2 and 3 a new approach for fitting which can incorporate the flux ratios at outset and which can permit an arbitrary azimuthal dependence for the surface density. Importantly, all the free parameters enter linearly into the models and so *the lens and flux ratio equations can always be solved by straightforward matrix inversion*. The models are only restricted by the fact that the surface mass density must be positive. This algorithm is used in section 4 to assess the evidence for anomalous flux ratios. Readers who are mainly interested in this application may skip section 3 entirely on the first reading. This section is rather mathematical and explicitly derives the linear equations for the parameters to be fitted.

2 SCALE-FREE MODELS

2.1 Potential and Surface Mass Density

Scale-free galaxy models with arbitrary power-law fall-off are widely used in galactic astronomy and dynamics (e.g., Toomre 1982; Evans 1994; Evans, Carollo & de Zeeuw 2000). The isophotes of a scale-free galaxy have the same shape at every radius and are completely described by a *shape function* $G(\theta)$, which depends only on the position angle θ with respect to the major axis. In such galaxies, the convergence κ and deflection potential ϕ are proportional to a power of r , namely

$$\kappa = \frac{1}{2}G(\theta)r^{\beta-2}, \quad \phi = r^\beta F(\theta). \quad (1)$$

Here, (r, θ) are familiar polar coordinates in the lens plane. The power is restricted to lie in the range $0 < \beta < 2$ for galaxy models. For $\beta < 0$, the mass at the centre of the galaxy does not converge. For $\beta > 2$, the surface mass density increases with radius, which is unrealistic. The important $\beta = 1$ case corresponds to an everywhere flat rotation curve.

In gravitational lensing, some simple scale-free potentials were already investigated by Kassiola & Kovner (1993). They were followed by Witt, Mao & Keeton (2000), who pointed out that the time delay is independent of the angular function $F(\theta)$ for the special case $\beta = 1$. Many applications to this general model followed (see Evans & Witt 2001; Zhao & Pronk 2001; Wucknitz 2002; Cardone et al. 2002).

From Poisson’s Law, we have

$$G(\theta) = \beta^2 F(\theta) + F''(\theta). \quad (2)$$

Given $F(\theta)$, it is straightforward to generate $G(\theta)$. However, it is also possible to solve this ordinary differential equation for $F(\theta)$ in terms of $G(\theta)$, as shown in Appendix A. This is useful, as it gives the scale-free potential corresponding to a given set of scale-free equidensity contours.

The critical curves can be given analytically. Using the determinant of the Jacobian, we obtain

$$\det J(r, \theta) = (\beta - 1)r^{2\beta-4}[\beta F F'' - (\beta - 1)F'^2 + \beta^2 F^2] - r^{\beta-2}[F'' + \beta^2 F] + 1 = 0. \quad (3)$$

Setting $\rho = r^{\beta-2}$ yields a quadratic equation in ρ which can easily be solved. The two roots correspond to the radial and the tangential critical curves respectively. They can be mapped onto the radial and tangential caustics with the lens equation using the components of the deflection angle (A2). For the flat rotation curve case ($\beta = 1$), the equation for the critical curve becomes linear and thus the caustic network is readily established, as shown in Evans & Witt (2001).

2.2 Fourier Expansions

Since $F(\theta)$ and $G(\theta)$ are periodic with period 2π , we can expand them as Fourier series (see e.g. Bronshtein & Semendyayev 1998). For convenience, we start with the potential $F(\theta)$ and write

$$F(\theta) = \frac{a_0}{2} + \sum_{k=1}^{\infty} [a_k \cos(k\theta) + b_k \sin(k\theta)]. \quad (4)$$

Using eq.(2), we obtain now for $G(\theta)$

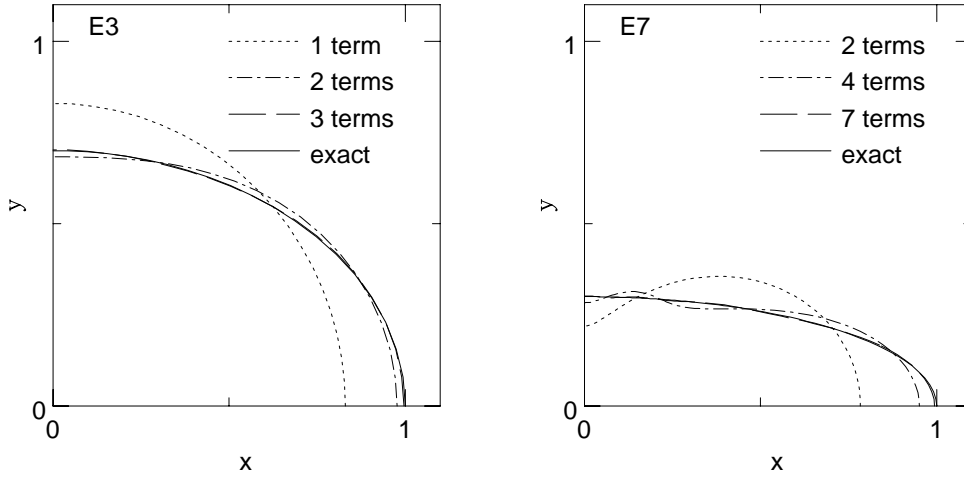


Figure 1. The two plots show truncated Fourier series approximations to the equidensity contours of an exactly elliptical E3 (left panel) and an E7 (right) galaxy. For moderate flattenings such as E3, excellent results are obtained with only the first three non-vanishing terms in the expansion. Even for the most highly flattened configurations such as E7, the approximation becomes very accurate when the first seven non-vanishing terms are included.

$$G(\theta) = \frac{a_0\beta^2}{2} + \sum_{k=1}^{\infty} [a_k(\beta^2 - k^2) \cos(k\theta) + b_k(\beta^2 - k^2) \sin(k\theta)]. \quad (5)$$

The coefficients in the Fourier series must obey the condition $G(\theta) \geq 0$ for all θ to obtain a positive surface mass density. After constructing a fit, this is easy to check *a posteriori*.

As an example, let us consider an elliptical surface mass density with a flat rotation curve ($\beta = 1$), which has

$$G(\theta) = A(\cos^2\theta + q^{-2}\sin^2\theta)^{-1/2}. \quad (6)$$

Since $G(\theta) = G(-\theta)$ is an even function, all b_k must vanish ($b_k = 0$). Since $G(\theta) = G(\pi - \theta)$, all a_k with k equal to an odd integer must also vanish. So, the only terms that remain in the Fourier series are the even integer cosine coefficients (cf. also Appendix B). Figure 1 shows how few terms are really required for accurate approximation. For an E3 galaxy, a Fourier series truncated after the first three non-vanishing terms already gives an excellent approximation to the true equidensity contours. Even for a highly flattened E7 galaxy, only the first seven non-vanishing terms are needed. This demonstrates that the Fourier expansions can give good results with few terms.

The advantage of the Fourier expansion is that it makes it very easy to solve the lens equation. For this reason, we list the Fourier coefficients for the popular elliptic density and potential models with flat rotation curves in Appendix B (although we do not need to use them in the main body of this paper).

2.3 The Image Positions and Fluxes

The lens equation relates the position of the source (ξ, η) to the positions of the image (x, y) through the derivative of the lensing potential (e.g., Schneider, Ehlers & Falco 1992)

$$\xi = x - \frac{\partial\phi}{\partial x}, \quad \eta = y - \frac{\partial\phi}{\partial y}. \quad (7)$$

Using polar coordinates in the image plane, the lens equation can be recast as

$$\xi = r \cos \theta - r^{\beta-1} [\beta \cos \theta F(\theta) - \sin \theta F'(\theta)], \quad (8)$$

$$\eta = r \sin \theta - r^{\beta-1} [\beta \sin \theta F(\theta) + \cos \theta F'(\theta)], \quad (9)$$

where we can express $F(\theta)$ and $F'(\theta)$ by Fourier series. Let us assume that we have measured the image positions (r_ℓ, θ_ℓ) (in polar coordinates) of a gravitational lens and inserted them into the lens equation. Immediately, we notice that all unknown quantities (i.e. ξ , η , and all a_i and b_i) enter linearly into the lens equation, except for β .

Let us now add the constraint that the magnification ratios of the images are equal to the observed values. Suppose that the ratio of the magnification of the ℓ th image to the k th is measured to be $f_{k\ell}$, then

$$f_{k\ell} = \frac{\det J(r_\ell, \theta_\ell)}{\det J(r_k, \theta_k)}, \quad (10)$$

where $\det J$ is given in eq. (3). We observe that the coefficients a_i and b_i enter in simple mixed quadratic form into the equations. However, for the special case of a flat rotation curve ($\beta = 1$), all unknown quantities enter linearly into the equation for the magnification relation.

In other words, *in the astrophysically important flat rotation curve case, the Fourier coefficients describing the lensing galaxy are related to the observables by a simple matrix equation.* This makes the problem of fitting to both the image positions and the flux ratios a straightforward matter of matrix inversion.

A number of recent investigations have exploited the well-known linearity of the lens equation to expand the potential in basis functions (e.g., Keeton 2001). Such methods can be a powerful way of exploring a large set of models, although the drawback is that some of the parameter space is often associated with the creation of additional images. The need to check for this can undermine the utility of starting

with such an algorithm. It is worthwhile emphasising how our work differs from such expansions. First, the fundamental and new contribution of our paper is that the flux ratio equation is linear for a galaxy with a flat rotation curve. Therefore, in our algorithm both the lens equations and the flux ratio equations are simultaneously solved. Second, the caustic network is straightforwardly available using the work in Section 2.1, and so it is very easy to check for the creation of unwanted additional images.

3 FITTING GRAVITATIONAL LENSES

3.1 A Singular Value Decomposition Problem

First, we insert the Fourier series of $F(\theta)$ into eqs. (8)–(9) to establish the linear equations for fitting for $\beta = 1$. Introducing a useful notation, we write for the lens equation

$$\xi(r, \theta) = r \cos \theta - \frac{a_0}{2} \alpha_0(\theta) - \sum_{k=1}^{\infty} [a_k \alpha_k(\theta) + b_k \beta_k(\theta)], \quad (11)$$

$$\eta(r, \theta) = r \sin \theta - \frac{a_0}{2} \hat{\alpha}_0(\theta) - \sum_{k=1}^{\infty} [a_k \hat{\alpha}_k(\theta) + b_k \hat{\beta}_k(\theta)], \quad (12)$$

where a_k and b_k are the Fourier coefficients of the unknown function $F(\theta)$, which describes the angular part of the potential. For the coefficients α_k and β_k , we find

$$\begin{aligned} \alpha_k(\theta) &= \cos \theta \cos(k\theta) + k \sin \theta \sin(k\theta), \\ \beta_k(\theta) &= \cos \theta \sin(k\theta) - k \sin \theta \cos(k\theta), \end{aligned} \quad (13)$$

and for $\hat{\alpha}_k$ and $\hat{\beta}_k$, we find

$$\begin{aligned} \hat{\alpha}_k(\theta) &= \sin \theta \cos(k\theta) - k \cos \theta \sin(k\theta), \\ \hat{\beta}_k(\theta) &= \sin \theta \sin(k\theta) + k \cos \theta \cos(k\theta), \end{aligned} \quad (14)$$

for all $k \geq 0$. The lens equations (8)–(9) must hold at the positions of the n images, given in polar coordinates as (r_ℓ, θ_ℓ) with $\ell = 1, \dots, n$. This provides $2n$ constraints on the unknown source position (ξ, η) and the unknown Fourier coefficients.

Now let us consider the magnification of the ℓ th image. For the flat rotation curve case ($\beta = 1$), we obtain

$$\det J = \frac{1}{p_\ell \mu_\ell} = 1 - \frac{G(\theta_\ell)}{r_\ell}, \quad (15)$$

where p_ℓ is the parity of the image ℓ . It is only the flux ratios that can be related to the observational data, not the magnifications themselves. For the flux ratio of image ℓ compared to image k , we obtain

$$f_{k\ell} = \frac{p_k \mu_k}{p_\ell \mu_\ell} = \frac{1 - G(\theta_\ell)/r_\ell}{1 - G(\theta_k)/r_k}. \quad (16)$$

The flux ratio may be positive or negative depending on the combination of parities of the images. For flux ratios, we always compare to a reference image, which without loss of generality we take to be the first image. As we take ratios, we only need to identify images of the same parity, which in a quadruplet lens are usually on opposite sides of the lensing galaxy. Clearing the fractions, we can write the equation in a similar form to the lens equation

$$(f_{1\ell} - 1)r_1 r_\ell = \frac{a_0}{2} \gamma_0(\theta_\ell) + \sum_{k=1}^{\infty} [a_k \gamma_k(\theta_\ell) + b_k \delta_k(\theta_\ell)], \quad (17)$$

with

$$\begin{aligned} \gamma_k(\theta_\ell) &= (1 - k^2)[f_{1\ell} r_\ell \cos(k\theta_1) - r_1 \cos(k\theta_\ell)] \\ \delta_k(\theta_\ell) &= (1 - k^2)[f_{1\ell} r_\ell \sin(k\theta_1) - r_1 \sin(k\theta_\ell)]. \end{aligned} \quad (18)$$

This provides a further $n - 1$ linear constraints on the unknowns.

Now let us introduce a compact notation to facilitate matters. We set $\alpha_{k\ell} \equiv \alpha_k(\theta_\ell)$, where the first index denotes the Fourier component and the second index the image number. Exactly similar definitions can be made for $\beta_{k\ell}, \hat{\alpha}_{k\ell}, \hat{\beta}_{k\ell}, \gamma_{k\ell}$ and $\delta_{k\ell}$. We are now ready to set up the matrix equation for the fitting to the positions of the images and the flux ratios. Let us write

$$C\mathbf{x} = \mathbf{d} \quad (19)$$

where

$$\mathbf{d} = (r_\ell \cos \theta_\ell, \dots, r_\ell \sin \theta_\ell, \dots, (f_{1\ell} - 1)r_1 r_\ell, \dots)^T \quad (20)$$

is a vector of $3n - 1$ observables. Here, ℓ runs from 1 to n for a lens system with n images. There is always one less equation for the flux constraints than for the image position constraints. The vector

$$\mathbf{x} = (\xi, \eta, a_0/2, a_1, b_1, a_2, b_2, \dots)^T \quad (21)$$

contains the unknown quantities, namely the source coordinates (ξ, η) , and the Fourier coefficients. There are in principle infinitely many such coefficients, but in practice the Fourier series is usually terminated so that \mathbf{x} is a vector of $3n - 1$ components as well. Finally, for the matrix C , we obtain

$$C = \begin{pmatrix} 1 & 0 & \alpha_{0\ell} & \alpha_{1\ell} & \beta_{1\ell} & \alpha_{2\ell} & \beta_{2\ell} & \dots \\ \cdot & \cdot & \cdot & \cdot & \cdot & \cdot & \cdot & \dots \\ 0 & 1 & \hat{\alpha}_{0\ell} & \hat{\alpha}_{1\ell} & \hat{\beta}_{1\ell} & \hat{\alpha}_{2\ell} & \hat{\beta}_{2\ell} & \dots \\ \cdot & \cdot & \cdot & \cdot & \cdot & \cdot & \cdot & \dots \\ 0 & 0 & \gamma_{0\ell} & \gamma_{1\ell} & \delta_{1\ell} & \gamma_{2\ell} & \delta_{2\ell} & \dots \\ \cdot & \cdot & \cdot & \cdot & \cdot & \cdot & \cdot & \dots \end{pmatrix} \quad (22)$$

Provided we can measure all n image positions and $n - 1$ flux ratios, then C has $3n - 1$ rows. The number of columns is in principle arbitrarily large, although in practice it usually makes sense to terminate the Fourier series so that C is a $3n - 1 \times 3n - 1$ matrix.

As it stands, the matrix C is always singular ($\det C = 0$). There exists a null space for the matrix C , i.e., there exists at least one non-vanishing vector \mathbf{x}_0 which satisfies the equation $C\mathbf{x}_0 = \mathbf{0}$. In fact, the matrix C has (at least) a two-dimensional null space. Fortunately, the null subspace can be easily constructed. Since $\alpha_{1\ell} = 1$, $\beta_{1\ell} = 0$, $\hat{\alpha}_{1\ell} = 0$, $\hat{\beta}_{1\ell} = 1$, $\gamma_{1\ell} = 0$ and $\delta_{1\ell} = 0$ for all ℓ , it is easy to verify that the null vector must be of the form $\mathbf{x}_0 = \lambda_1 \mathbf{v}_1 + \lambda_2 \mathbf{v}_2$ with $\mathbf{v}_1 = (1, 0, 0, -1, 0, \dots)^T$ and $\mathbf{v}_2 = (0, 1, 0, 0, -1, 0, \dots)^T$.

From the physical point of view, the Fourier coefficients a_1 and b_1 simply produce a shift or transformation of the source position (ξ, η) . However, both coefficients do not contribute to the surface mass density for the special case of $\beta = 1$ since $a_1 \cos \theta$ and $b_1 \sin \theta$ are solutions of the homogeneous differential equation $F(\theta) + F''(\theta) = 0$ (cf. eq.(2)). We can excise this degeneracy by simply setting $a_1 = b_1 = 0$, which corresponds to the choice of origin. Now we can just remove the 4th and 5th column of the matrix C and add two higher degree Fourier coefficients to the problem to maintain C as a $3n - 1 \times 3n - 1$ matrix. The new matrix is usually

	$-\Delta\alpha$ (in $''$)	$\Delta\delta$ (in $''$)	Radio fluxes (in μ Jy)	Mid-infrared flux fractions	H band (in mags)	I band (in mags)
A	0.0	0.0	65.5 ± 8.4	0.27 ± 0.02	14.96 ± 0.06	15.92 ± 0.12
B	0.673 ± 0.003	1.697 ± 0.003	64.2 ± 8.4	0.30 ± 0.02	15.46 ± 0.02	17.21 ± 0.11
C	-0.635 ± 0.003	1.210 ± 0.003	26.5 ± 8.4	0.16 ± 0.02	15.71 ± 0.03	16.77 ± 0.12
D	0.866 ± 0.003	0.528 ± 0.003	59.4 ± 8.4	0.27 ± 0.02	16.00 ± 0.04	17.39 ± 0.04
G	0.075 ± 0.004	0.939 ± 0.003				

Table 1. Observational data on the Einstein Cross. The optical positions are taken from the CASTLES survey, as are the H and I band fluxes. The radio fluxes are provided by Falco et al. (1996). The mid-infrared flux fractions are given in Agol, Jones & Blaes (2000).

Band	ξ	η	a_0	a_2	b_2	a_3	b_3	a_4	b_4	a_5	b_5
Radio	0.0698	-0.0134	1.7748	-0.0422	0.0430	0.0004	-0.0017	0.0007	0.0012	0.0000	0.0008
Mid-IR	0.0662	-0.0131	1.7711	-0.0417	0.0417	0.0000	0.0002	0.0009	0.0005	-0.0002	0.0001
I	0.0689	-0.0142	1.7670	-0.0368	0.0477	-0.0043	0.0018	-0.0016	-0.0018	0.0029	0.0029
H	0.0640	-0.0132	1.7718	-0.0392	0.0448	-0.0013	0.0011	0.0002	0.0004	0.0019	0.0025

Table 2. Fourier coefficients of the solutions for the Einstein Cross. They correspond to the bold lines in Figure 2, for which the positions and flux ratios are reproduced within the errors and are given in the same coordinate system as the data in Table 1 but translated to the lens centre.

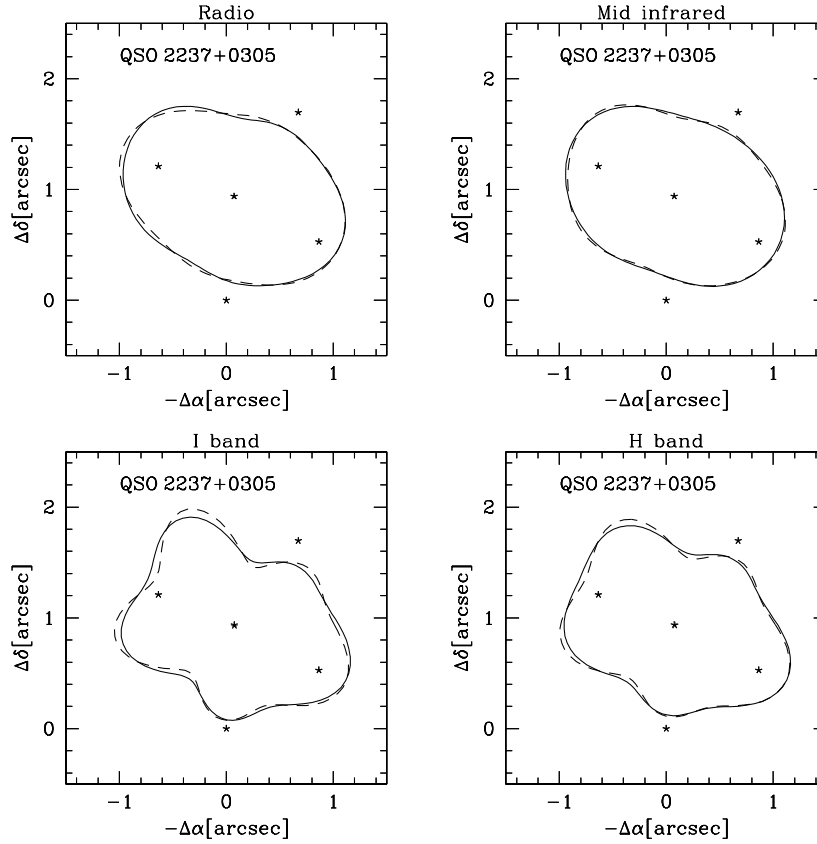


Figure 2. Each panel shows in a dashed line the critical curve (which is also an equidensity contour when the rotation curve is flat) of a lens model for the Einstein Cross that exactly fits the image positions and the flux ratios. The full curve shows the equidensity contour of a model that fits the data within the uncertainties. Working clockwise from the top left, the panels use the flux ratios in the radio, mid infrared, H band and I band respectively. The locations of the four images and the lensing galaxy are also marked.

	$-\Delta\alpha$ (in $''$)		$\Delta\delta$ (in $''$)		Radio Fluxes	
	Predicted	Observed	Predicted	Observed	Predicted	Observed
A	0.0	0.0	0.0	0.0	65.5	65.5
B	0.673	0.673	1.697	1.697	61.1	64.2
C	-0.635	-0.635	1.210	1.210	27.9	26.5
D	0.866	0.866	0.528	0.528	56.6	59.4
G	0.070	(0.075)	0.939	(0.939)	—	—

	$-\Delta\alpha$ (in $''$)		$\Delta\delta$ (in $''$)		Mid-infrared flux fractions	
	Predicted	Observed	Predicted	Observed	Predicted	Observed
A	0.0	0.0	0.0	0.0	0.27	0.27
B	0.673	0.673	1.697	1.697	0.27	0.30
C	-0.635	-0.635	1.210	1.210	0.15	0.16
D	0.866	0.866	0.528	0.528	0.30	0.27
G	0.075	(0.075)	0.939	(0.939)	—	—

Table 3. Predicted and observed quantities for two of the solutions of the Einstein Cross given in Figure 2. The upper (or lower) panel corresponds to the lens model with equidensity contour given by the bold curve in the panel for the radio (or mid-infrared fluxes). The positions $-\Delta\alpha$ and $\Delta\delta$ are computed relative to image A. Notice that all the data are well-reproduced within even the formal uncertainties and the flux ratios are not anomalous.

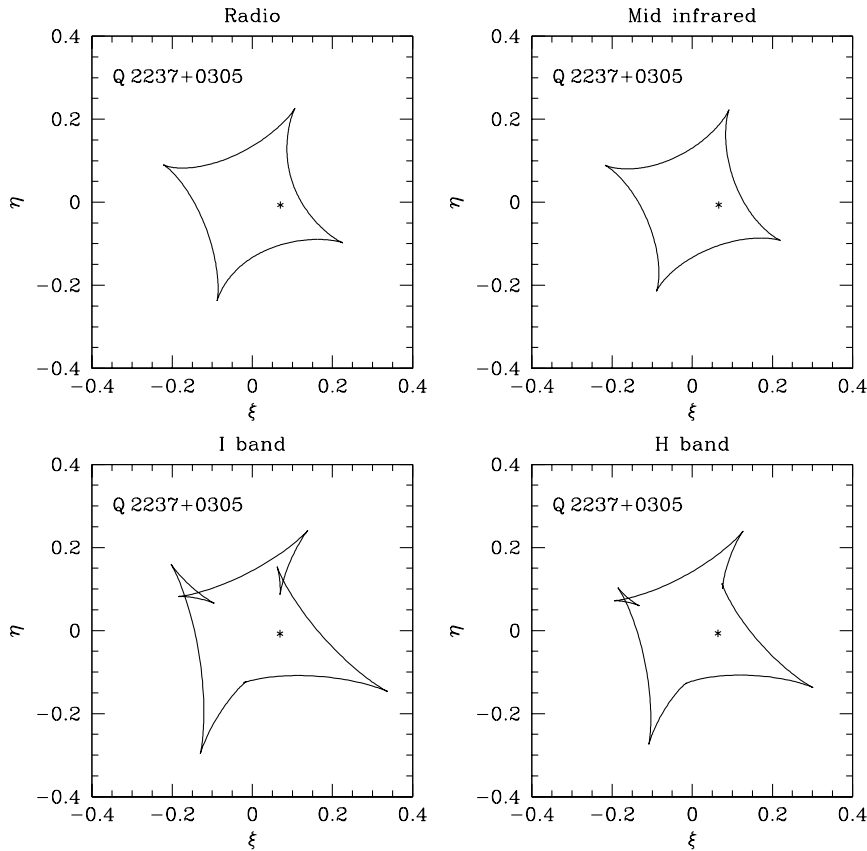


Figure 3. The panels show the caustics of the Einstein Cross corresponding to the exact solutions (dashed curves in Fig. 2). The computed position of the lensed quasar is indicated. It always lies in the region of 4 images. For the I and H band, there are butterfly and swallowtail cusps (small regions of the source plane where 6 images may occur).

non-singular and so a Gauss-Jordan elimination can formally solve the problem. However, it is better to use singular value decomposition (SVD) to solve for the unknown vector \mathbf{x} (cf. Press et al. 1999). In this way, we are always guaranteed to find a numerically stable solution.

The singular value decomposition of the matrix C is

$$C = U \cdot W \cdot V^T, \quad (23)$$

where the $3n-1 \times 3n-1$ matrices U and V are orthonormal, and the matrix W is a diagonal matrix of singular values $(w_1, w_2, \dots, w_{3n-1})$. As usual in a singular value decomposition (SVD), any very small singular values are removed (see Press et al. 1989) and this must be accompanied by a corresponding reduction in the number of unknown Fourier coefficients. Typically, any singular value whose ratio to the largest singular value is less than 10^{-4} is removed. After deletion, let us suppose that m singular values remain, where $m \leq 3n - 1$. If $m = 3n - 1$, then the SVD solution is exact; if singular values are removed, then the solution is usually very good.

Let us remark here that one can add further higher degree Fourier coefficients and then the fitting problem becomes underdetermined. We can obtain a whole space of models all of which would equally well reproduce the observed data. It is clear – even with the severe restriction that we have made to a scale-free model with a flat rotation curve – that the variety of models that fit the data is extremely large. This cautions us against making rash statements based on goodness-of-fit to a single model.

3.2 Uncertainties

It is of modest interest to provide a model that fits the observational data exactly, as the uncertainties in the flux ratios may be substantial. It is of much greater interest to be able to find a set of models that can reproduce the data within the errors.

The relative image positions are usually known to extremely high accuracy. For lenses observed with the *Hubble Space Telescope*, the error in the relative astrometry is only ~ 3 mas. From the point of view of modelling, however, the important quantities are the relative positions of the images with respect to the centre of the mass distribution of the lensing galaxy. These coordinates are less accurately determined. The centre of the light distribution of the lensing galaxy is sometimes poorly known (especially if it is at high redshift). In any case, there is no guarantee that the center of the light corresponds to the centre of the mass. In our modelling, we always reproduce the relative image positions exactly, but we allow for an error of no more than 50 mas in the position of the center of the lens.

For the flux ratios, we distinguish between the radio and the optical data. The flux measurements in the radio may be affected by scintillation or scatter-broadening or free-free absorption. An isolated example of radio microlensing is known (Koopmans & de Bruyn 2000), but the effects of microlensing are not generally believed to be substantial in the radio. Whenever we use radio data, we assume that the typical uncertainty in the flux ratio is no more than 5 per cent. However, there are much greater problems in the optical bands. Each image might be affected by differential extinction or by microlensing. Microlensing can cause

an image to be below or above its average magnification for decades (see Witt & Mao 1994 for an extensive discussion of the effects of microlensing). The recent years have seen monitoring campaigns of both Q 2237+030 and Q 0957+561, which provide irrefutable evidence for microlensing (Colley et al. 2000; Wozniak et al. 2002; Schmidt et al. 2002). There are at least a further five multiply imaged quasars for which evidence exists implicating microlensing in the optical (HE 1104-1805, PG 1115+080, H 1413+117, B 0218+357, B 1600+434). Therefore, the optical flux ratios are more uncertain and we assume that they have an error of $\lesssim 10$ per cent.

3.3 Position Angle of the Lensing Galaxy Axes

The axes of the local right ascension and declination coordinates may be rotated by an arbitrary angle with respect to the major and minor axes of the lensing galaxy. This is implicitly contained in the derived Fourier coefficients.

We can expand the Fourier series as

$$\begin{aligned} & \sum_{k=1}^{\infty} [a_k \cos(k\theta) + b_k \sin(k\theta)] \\ &= \sum_{k=1}^{\infty} [a_k^R \cos(k\theta + k\theta_R) + b_k^R \sin(k\theta + k\theta_R)], \end{aligned} \quad (24)$$

where θ_R is the rotation angle and a_k^R and b_k^R are the Fourier coefficients in the rotated coordinate system. It is easy to verify that

$$\begin{aligned} a_k^R &= a_k \cos k\theta_R + b_k \sin k\theta_R \\ b_k^R &= -a_k \sin k\theta_R + b_k \cos k\theta_R. \end{aligned} \quad (25)$$

If the lensing galaxy has a major axis, the following condition must be satisfied:

$$G'(\theta_R) \approx 0 \approx G'(\theta_R + 180^\circ). \quad (26)$$

If the lensing galaxy looks regular, it probably has, in addition to a major axis, an approximate reflection symmetry $G(\theta) \approx G(-\theta)$, or equivalently $F(\theta) \approx F(-\theta)$. Therefore, in the rotated system, we expect $b_k^R \approx 0$ for all k . In other words, the rotated system is defined by

$$\sum_{k=1}^n (b_k^R)^2 = \text{minimum}. \quad (27)$$

Solving this equation yields the rotation angle of the major axis of the lensing galaxy

$$2 \sum_{k=1}^n k a_k b_k \cos(2k\theta_R) = \sum_{k=1}^n k (a_k^2 - b_k^2) \sin(2k\theta_R). \quad (28)$$

This equation must in general be solved numerically. For galaxy-like mass distributions, the dominant higher-order terms in the Fourier expansion are those with $k = 2$ and then the solution is analytic, namely

$$\tan 2\theta_R = \frac{b_2}{a_2}. \quad (29)$$

For applications to individual lenses, we note that the position angle as conventionally defined by astronomers (North through East) is $90^\circ - \theta_R$.

	$-\Delta\alpha$ (in ")	$\Delta\delta$ (in ")	I band (K93) (in mags)	H band (in mags)	V band (in mags)	I band (in mags)
A1	-1.328 ± 0.004	-2.034 ± 0.004	16.12	15.71 ± 0.03	16.90 ± 0.11	16.42 ± 0.02
A2	-1.477 ± 0.004	-1.576 ± 0.003	16.51	16.21 ± 0.04	17.62 ± 0.09	16.85 ± 0.03
B	0.341 ± 0.003	-1.961 ± 0.004	18.08	17.70 ± 0.05	18.39 ± 0.45	17.91 ± 0.39
C	0	0	17.58	17.23 ± 0.04	18.95 ± 0.32	18.37 ± 0.34
G	-0.381 ± 0.003	-1.344 ± 0.003				

Table 4. Observational data on the quadruplet PG 1115+080. The optical positions are taken from the CASTLES survey, as are the V,H and I band fluxes. For comparison, we also give the earlier I band fluxes found by Kristian et al. (1993).

Band	ξ	η	a_0	a_2	b_2	a_3	b_3	a_4	b_4
H	-0.0273	0.1122	2.2946	-0.0029	0.0052	-0.0021	0.0027	-0.0007	-0.0002
I (K93)	-0.0277	0.1114	2.3039	0.0007	0.0059	0.0013	0.0060	0.0000	0.0020
V	-0.0238	0.1175	2.2871	-0.0081	0.0035	-0.0054	-0.0001	-0.0022	-0.0020
I	-0.0218	0.1145	2.2880	-0.0064	0.0034	-0.0049	0.0001	-0.0016	-0.0012

Table 5. Fourier coefficients of the solutions for PG 1115+080, assuming a constant external shear with a magnitude of 0.103 and a direction of 65.8° measured from west to north (following Schechter et al. 1997). The coefficients are computed in the same coordinate system as the data in Table 4 but translated to the lens centre.

3.4 Mass inside the Einstein Ring

Evans & Witt (2001) showed that the mass inside the Einstein ring must be very close to the mass inside the critical curve for the special case of $\beta = 1$, and can be written as

$$M_E \approx M_{\text{crit.curve}} = \frac{1}{2\pi} \int_0^{2\pi} G^2(\theta) d\theta. \quad (30)$$

We therefore deduce that

$$M_E \approx \frac{a_0^2}{4} + \sum_{i=2}^N (k^2 - 1)^2 (a_k^2 + b_k^2). \quad (31)$$

To apply this to a real lens, we have to scale the result by the factor $\Sigma_{\text{crit}} D_d^2$ containing the normalized surface mass density which is given by

$$\Sigma_{\text{crit}} = \frac{c^2 D_s}{4\pi G D_d D_{\text{ds}}}. \quad (32)$$

Here, D_d , D_s and D_{ds} are the distance to the deflector, the distance to the source and the distance from the deflector to the source respectively. Given the redshift of the lens and the source, this (32) enables the projected mass within the Einstein ring to be estimated.

4 AN APPLICATION: ANOMALOUS FLUX RATIOS

In this section, we consider three of the lens systems for which substructure has been claimed either by Metcalf & Zhao (2002) or by Dalal & Kochanek (2002) or by Chiba (2002).

4.1 Q 2237+030 (The Einstein Cross)

The data on the four images of Q 2237+030 (the Einstein Cross) are listed in Table 1. Much of this comes from the

CASTLES survey^{*}. Q 2237+030 is an unusual lens because so much more information is available for the lensing galaxy than is customary. In particular, the redshift of the lens is so small ($z = 0.039$) that the galaxy's light distribution can be measured (e.g., Wyithe et al. 2002). The lens is a face-on barred galaxy (e.g., Schmidt, Webster & Lewis 1998). The optical fluxes are known to be affected by microlensing (Irwin et al. 1989; Wambsganss, Schneider & Paczyński 1990; Wozniak et al. 2000), which causes each image to differ from the average magnification. Typically, we expect that the images are very likely below the average magnification if they are in a quiescent state (for years), while the images are very likely above the average magnification if they are in a more active state (cf. Witt & Mao 1994).

It is often argued that the radio and mid-infrared fluxes are more reliable because the source emitting region is more extended and therefore less affected by microlensing. If this is the case, then gravitational lens models should use the radio and mid-infrared flux ratios in preference to optical. The flux ratios in the radio were measured by Falco et al. (1996) with a signal-to-noise of $\sim 2 - 4$. The mid-infrared flux ratios have recently become available thanks to Agol, Jones & Blaes (2000). The flux ratios in radio and mid-infrared are in good agreement, but differ from the optical flux ratios.

Figure 2 shows the critical curves for four models of Q 2237+030. From eq. (15), the critical curve is also an equidensity contour when the rotation curve is flat. As the models are scale-free, the equidensity contours retain the same shape independent of position, although the size of course varies. In each case, the dashed curve describes a model that exactly reproduces the image positions and flux ratios. It is found by solution of the matrix equation (19) using singular value decomposition (SVD). Figure 3 shows

^{*} <http://cfa-www.harvard.edu/castles/>

	$-\Delta\alpha$ (in $''$)		$\Delta\delta$ (in $''$)		H band fluxes (in mags)	
	Predicted	Observed	Predicted	Observed	Predicted	Observed
A1	-1.324	-1.328	-2.035	-2.034	15.71	15.71
A2	-1.481	-1.477	-1.575	-1.576	16.10	16.21
B	0.341	0.341	-1.961	-1.961	17.59	17.70
C	0	0	0	0	17.33	17.23
G	-0.391	(-0.381)	-1.334	(-1.344)	–	–

	$-\Delta\alpha$ (in $''$)		$\Delta\delta$ (in $''$)		I band fluxes of K93 (in mags)	
	Predicted	Observed	Predicted	Observed	Predicted	Observed
A1	-1.324	-1.328	-2.035	-2.034	16.12	16.12
A2	-1.481	-1.477	-1.575	-1.576	16.40	16.51
B	0.341	0.341	-1.961	-1.961	18.18	18.08
C	0	0	0	0	17.47	17.58
G	-0.386	(-0.381)	-1.329	(-1.344)	–	–

Table 6. Predicted and observed quantities for two of the solutions given in Figure 4. The upper (or lower) panel corresponds to the lens model with equidensity contour given by the bold curve in the panel for the H band (or I band of K93) fluxes. The positions $-\Delta\alpha$ and $\Delta\delta$ are computed relative to image C. Notice that astrometric data are well-reproduced within even the formal uncertainties whilst the flux ratios are not anomalous, once an uncertainty of 10 per cent is allowed for the effects of microlensing.

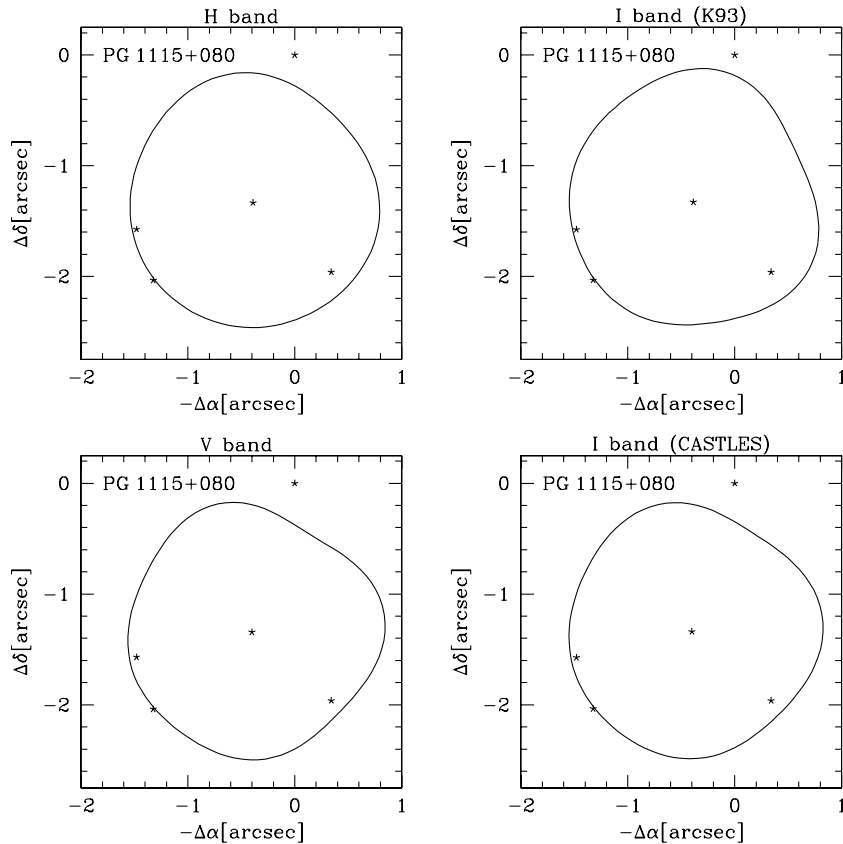


Figure 4. The panels show the equidensity contours ($\kappa = 1/2$) for lens models of PG 1115+080. The bold curves reproduce the relative astrometry within the errors and the measured optical flux ratios to better than 10 per cent. As a constant external shear is assumed, the equidensity contour is no longer a critical curve. The locations of the four images and the lensing galaxy are also marked.

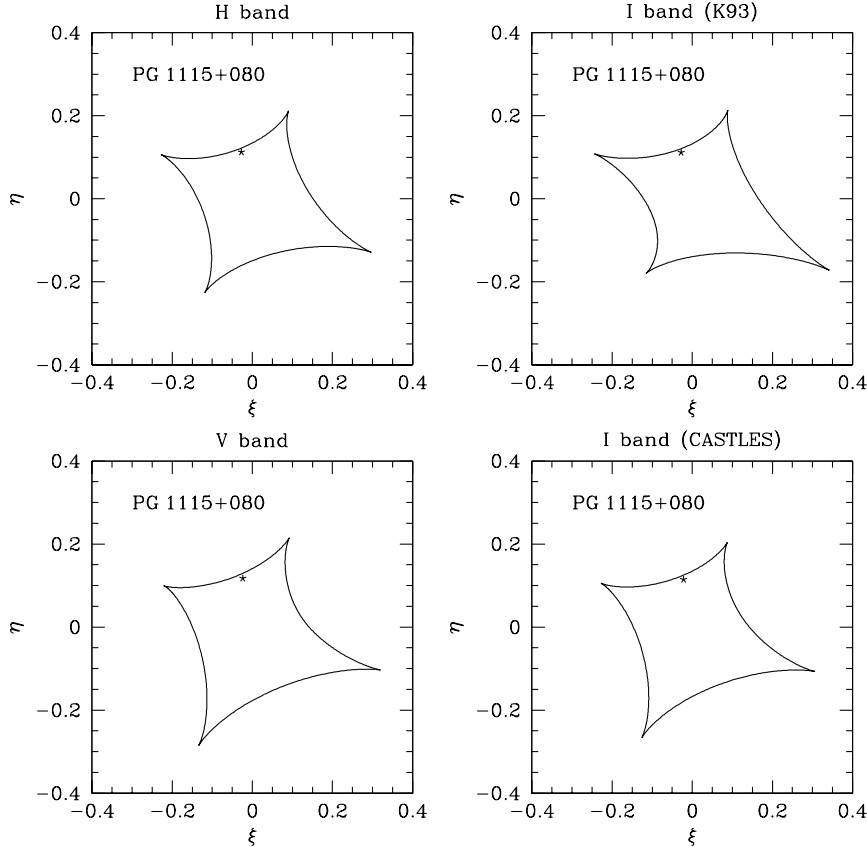


Figure 5. The panels show the caustics of the lens model for PG 1115+080 corresponding to the solutions in Fig. 4. The computed position of the lensed quasar is indicated. It always lies in the region of 4 images. There are no regions in which higher order imaging occurs (butterfly and swallowtail cusps).

the corresponding caustics of the exact solutions of the critical curves (dashed lines). The more irregular critical curves (I and H band data) correspond to caustics with over-folds like swallowtails and butterflies. However, in each case, the source position still lies inside the four image region. Unwanted extra images are not produced.

We assume that the measured flux ratios in the optical band are in error by $\lesssim 10$ per cent due to microlensing. The relative positions of the image are always maintained within the formal errors (given in Table 1), but the center of the lensing galaxy may be displaced by up to 50 mas. We find the model for which

$$b_2^2 + \sum_{i \geq 3} [a_i^2 + b_i^2] \quad (33)$$

is minimised. This suppresses Fourier components higher than the bar-like $m = 2$ component. In other words, out of all the solutions that reproduce the data, we choose the one that most looks like a galaxy. The models so produced are shown in bold lines in Figure 2; the details of the solutions are listed in Table 2. Finally, for two of the bold line solutions, we show how the image positions and the flux ratios are reproduced in Table 3. All the observable quantities are extremely well reproduced by the model, including the flux ratios.

Two points emerge clearly from this. First, the equidensity contours implied by reproducing the exact radio or mid-infrared fluxes are already in good agreement. The position angle of the lensing galaxy as inferred from eq. (26) using the radio or mid-infrared solutions is $\sim 67.3^\circ$ (measured from North through East). For comparison, Trott & Webster (2002) report that the position angle of the bar in the lensing galaxy is $\sim 39^\circ$, while the major axis of the galaxy in its outer parts is $\sim 77^\circ$. Second, the equidensity contours implied by exactly reproducing the I and the H band optical flux ratios are distorted. However, there are more regular solutions once an allowance is made for the effects of microlensing on the flux ratios.

Distortions of isophotes from elliptical form are generally given in terms of Bender et al.'s (1989) coefficients. These are usually calculated for early-type galaxies and have absolute values less than 0.05 (see e.g., Binney & Merrifield 1998, section 4.3). In fact, barred galaxies, such as the lens in Q 2237+030, may have substantially larger deviations, which moreover depend on position along the major axis. The method of calculating these coefficients for densities given as Fourier expansions is elaborated in Appendix C; we quote the results here. For the radio contours, Bender's coefficients are $a_3^B/a_0 = -0.008$ and $a_4^B/a_0 = -0.005$; for the mid-infrared, they are $a_3^B/a_0 = 0.001$ and $a_4^B/a_0 = -0.011$.

These values are well within the observed range, emphasising that our solutions for the shapes of the equidensity contours are realistic. By comparison, for the distorted I band contours, the coefficients are $a_3^B/a_0 = 0.012$ and $a_4^B/a_0 = -0.034$.

All this provides strong evidence for the point of view advanced in Agol et al. (2000) that the radio and mid-infrared fluxes are trustworthy and that the optical flux ratios are discrepant because of microlensing. All the data are internally consistent and once reasonable error bars are placed on the flux ratios, there is no need to invoke substructure to explain the data (c.f. Metcalf & Zhao 2002).

4.2 PG 1115+080

Let us now examine the lens system PG 1115+080, which has been claimed to provide evidence for substructure by Dalal & Kochanek (2002), Metcalf & Zhao (2002) and Chiba (2002). The observational data on PG 1115+080 are listed in Table 4. The I, V and H band fluxes are provided from the CASTLES survey. There is also earlier data on the I band fluxes thanks to Kristian et al. (1993, hereafter K93).

There is already evidence that the flux ratios may come with substantial uncertainties. For example, Foy, Bonneau & Blazit (1985) found component A2 of PG 1115+080 was brighter than A1 in 1984 March-May, whereas most subsequent investigators have found A2 to be fainter than A1. The conclusion advanced by Christian, Crabtree & Waddell (1987) is that the images in PG 1115+080 are being affected either by microlensing or by time-delayed intrinsic variations in the quasar or both. Witt, Mao & Schechter (1995) showed that the likelihood of observing microlensing in images A1 and A2 is much higher than in C and D. Notice too that the CASTLES and the Kristian et al (1993) I band fluxes in Table 4 are not consistent within the stated error bars, the discrepancies almost certainly being due to microlensing. Radio emission would be less affected by microlensing, but PG 1115+080 is radio-quiet and so the optical fluxes have to be used.

Impey et al. (1998) have carried out deep *Hubble Space Telescope* imaging of PG 1115+080 in the infrared. They found that the primary lens is a nearly round elliptical galaxy with an ellipticity of less than 0.07. The lens is part of a group of galaxies, whose effects must be included in successful models. The group is modelled by a uniform external shear with a magnitude of 0.103 and a direction of 65.8° measured from west to north, following Schechter et al. (1997). The extension of our SVD method to the case of uniform shear is sketched in Appendix D. We implement our fitting procedure, deleting two singular values for numerical stability and finding the solution that minimises (33), but still reproduces the data within our assumed errors. The panels of Figure 4 show the equidensity contours of the resulting models. Again, the relative astrometry of the images is recovered to within the formal error (~ 4 mas), the lens centre may be misligned by up to 50 mas, while the optical flux ratios are reproduced to within 10 per cent. The comparison between model predictions and observed quantities for the H and I band (K93) solutions are given in Table 6. The contours implied by reproducing the H or I band (K93) fluxes are in good agreement and look plausibly like the projected mass distribution of a very round early-type galaxy, in ac-

cordance with Impey et al.'s (1998) imaging. There is some slight distortion in the equidensity contours that reproduce the V or I band (CASTLES) flux ratios. The caustic networks are shown in Figure 5 to demonstrate that unwanted extra images are not formed.

Again, the shapes of the equidensity contours in Figure 4 do exhibit small deviations from pure elliptical form, which can be quantified by Bender et al.'s (1989) coefficients. Using the method of Appendix C, we find $a_3^B/a_0 = 0.009$ and $a_4^B/a_0 = -0.004$ for the H band and $a_3^B/a_0 = -0.015$ and $a_4^B/a_0 = -0.004$ for the I band (K93) contours. There is some data on the shapes of dark haloes of spiral galaxies from numerical simulations (e.g., Heyl, Hernquist & Spergel 1994), which supports the notion that $|a_3| \lesssim 0.05$ and $|a_4| \lesssim 0.05$. So, the amplitudes of the higher order terms in our solutions for the lens galaxy do lie easily within the range expected for dark haloes of spiral galaxies.

It is clear from the smooth models that we have constructed that there is no really compelling evidence for substructure in this lens at the moment, despite abundant claims to the contrary (Dalal & Kochanek 2002; Metcalf & Zhao 2002; Chiba 2002; Kochanek & Dalal 2003). There are smooth and realistic models that do fit the data within the likely uncertainties.

4.3 B 1422+231

Patnaik et al. (1992) discovered the gravitational lens B 1422+231 in a radio survey. Table 7 lists some of the available data on the images, largely provided by the CASTLES group. It was realised by both Hogg & Blandford (1994) and Kormann, Schneider & Bartelmann (1994) that it is difficult to reproduce the flux ratios of this lens system with a simple model. Hogg & Blandford used a mixture of isothermal spheres and point masses whereas Kormann et al. used a model with external shear. The latter strategy has been followed by most modern modellers.

Using our SVD method, it was impossible to reproduce the reported errors in the relative astrometry, together with the assumed uncertainties in the flux ratios (5 per cent for the radio, 10 per cent for the optical) at least with physical models. Unphysical models are readily identified as the equidensity contours are self-intersecting. Accordingly, for this lens only, the errors in the relative astrometry were inflated by a factor of 10 to ~ 30 mas. Figure 6 now shows the results of our fitting procedure in four flux bands, but none of the results can be said to be at all satisfactory. The equidensity contours are strongly distorted from those expected in galaxy-like models. Just as alarming as the shape of the contours is the fact that the fitted parameters do not have consistent values from one band to the next.

The conclusion to be drawn by the failure of the fitting procedure is that – even taking into account observational uncertainties – this lens system requires additional ingredients. Possibly, as Mao & Schneider (1998) were the first to suggest, substructure may be causing a dramatic effect on the flux ratios. Possibly, as Kundic et al. (1997) suggest, the effects of external shear caused by nearby galaxies and clusters of galaxies may also need to be included in the analysis.

	$-\Delta\alpha$ (in $''$)	$\Delta\delta$ (in $''$)	Radio fluxes (in μ Jy)	r band (in mags)	V band (in mags)	H band (in mags)
A	0.0	0.0	216	16.77	16.43 ± 0.11	14.41 ± 0.03
B	0.385 ± 0.003	-0.317 ± 0.003	221	16.45	16.45 ± 0.10	14.29 ± 0.03
C	0.722 ± 0.003	-1.068 ± 0.003	115	17.25	17.09 ± 0.07	14.98 ± 0.03
D	-0.562 ± 0.004	-1.120 ± 0.003	4.5	20.40	20.44 ± 0.06	18.14 ± 0.04
G	-0.375 ± 0.004	-0.973 ± 0.004				

Table 7. Observational data on the quadruplet B 1422+231. The optical positions are taken from the CASTLES survey, as are the H and V band fluxes. The radio fluxes are provided by Patnaik et al. (1992).

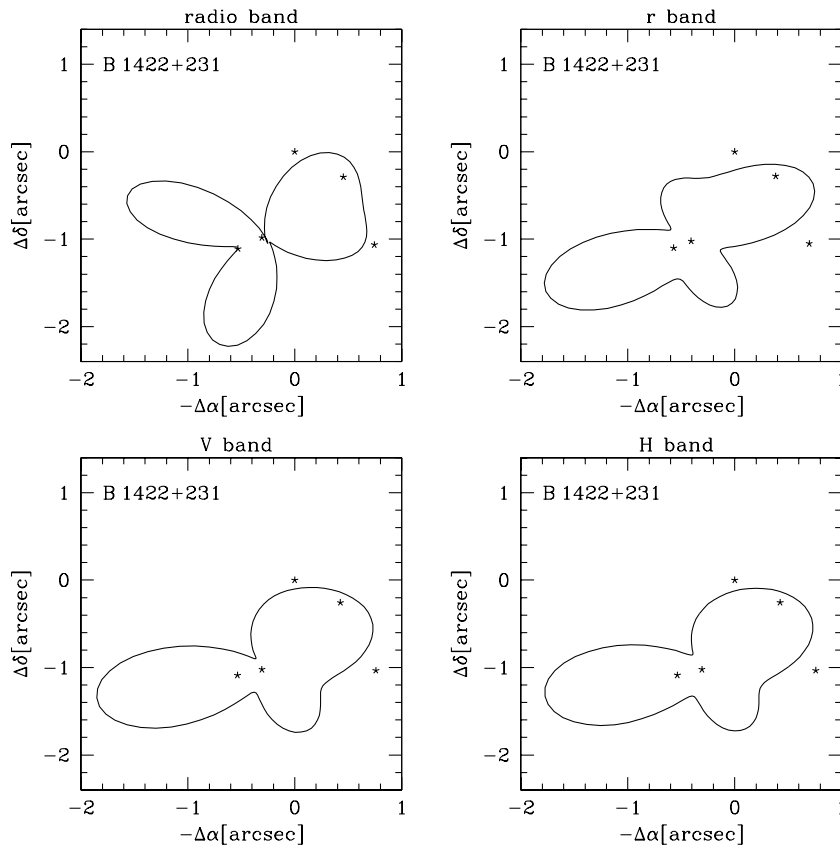


Figure 6. The panels show the equidensity contours (or critical curves) for the quadruplet system B 1422+231. Working clockwise from the top left, the panels use the flux ratios in the H band, r band, V band and radio. This is a lens for which substructure may well be present, as none of our models are at all satisfactory.

5 DISCUSSION

The main aim of this paper is to present a new, simple approach to fitting a model to the data on a gravitational lens. Given the image positions and the flux ratios (if available), a model that exactly fits that data can be constructed by a simple matrix inversion (preferably by singular value decomposition, available in standard numerical libraries). All the fitting parameters enter linearly into the equation. No complicated non-linear χ^2 -fitting needs to be done.

The lensing galaxy is always assumed to be scale-free with a flat rotation curve. There is already a substantial body of evidence from fitting of lenses that early-type galax-

ies have nearly isothermal profiles (Kochanek 1995; Muñoz et al. 2001; Cohn et al. 2001; Rusin et al. 2002). In particular, the absence of central images strongly constrains the lensing potential of early-type galaxies to be isothermal or steeper and the size of any core region to be small (e.g., Rusin & Ma 2001; Evans & Hunter 2002). There is both stellar dynamical (e.g., Gerhard et al. 2001) and X-ray (Fabbiano 1997) evidence that early-type galaxies have flat rotation curves out to at least 4 effective radii. Hence, our assumption of a flat rotation curve seems exactly what the data require.

Unusually, our algorithm allows full flexibility as regards the angular structure of the lensing potential. Earlier

fitting procedures have allowed the lensing potential to have different radial structure (for example, different power-law profiles), but usually only simple forms of angular structure (for example, constant external shear). In our models, the radial structure is always fixed as isothermal, but the shape of the density contours is completely arbitrary. The lens model has a flexible number of free parameters, and of course includes the isothermal elliptic density and potential models which have a distinguished history in gravitational lens modelling. The fit allows direct deduction of the mass contour of the lensing galaxy. Although we have presented examples based on quadruplet lens systems, the algorithm can be adapted for a two image or a higher image model. A higher image model might be needed, for example, in Q0957+561, where 10 sub-image positions can be detected in the radio band. Another good application might be MG 0414+0534, where some substructure of the images are detected (cf. Trotter, Winn & Hewitt 2000 and their fitting approach). Both lenses seem heavily distorted by external shear. A shear term can be added to our algorithm. If the shear is known, then the lens and flux ratio equations remain linear.

The flux ratios may enter directly into the fit depending on whether they are available or trustworthy. We stress that flux ratios often do not provide good model constraints. The reason for this is easy to understand. The flux ratios depend on the second derivatives of the lensing potential, whereas time delays and image positions are proportional to the potential and its first derivative respectively. Therefore, flux ratios are particularly sensitive to graininess in the gravitational potential. This often manifests itself as microlensing. The flux ratios are also affected by the uncertain differential extinction corrections that must be applied to each image. Radio and mid-infrared fluxes are generally more reliable than optical. However, effects such as scintillation, scatter-broadening and free-free absorption may affect the radio fluxes in some of the lenses. If flux ratios are incorporated into a fit, it is vital that there is a realistic treatment of the errors.

Our fitting algorithm permits the construction of a whole class of degenerate models all of which can fit the image position and flux ratios exactly. In addition, the models are also degenerate in the time delay since the delay depends only on the distance of the image positions to the centre of the lensing galaxy (cf. Witt, Mao & Keeton 2000). Such degeneracy is easy to understand pictorially. Given a Fermat time delay surface, we need only keep the values, the derivatives and the second derivatives of the surface at the image positions fixed. We then have enormous freedom to move the surface (subject only to the constraints that no additional images are introduced and that no negative mass density is produced).

We have used our new fitting algorithm to examine critically some of the claims made recently for anomalous flux ratios. The procedure used by both Dalal & Kochanek (2002) and Metcalf & Zhao (2002) was to show that a family of simple models did not reproduce the flux ratios. However, it does not follow from this that substructure is necessary; it may just be that the simple model did not have enough flexibility to provide a good match. For example, of the five lenses studied by Metcalf & Zhao (2002), they themselves concluded that one (MG 0414+0534) could be satisfacto-

rily explained by a smooth model. In this paper, we have demonstrated that the data on two others (PG 1115+080, Q 2237+030) are consistent with smooth galaxy-like models, especially when a realistic treatment of the errors in the flux ratios is incorporated.

We note that the fraction of mass in substructure expected in galaxy haloes is very small ($\lesssim 5$ per cent) and it occurs overwhelmingly in the outlying portions (e.g., Moore et al. 1999; Ghigna et al. 2000). Substructure evolves as it is subjected to tides, impulsive collisions and dynamical friction. Tidal disruption becomes important as soon as the mean density of the galaxy is equal to the density of the substructure. Similarly, the dynamical friction timescale scales with the square of the galactocentric radius (see e.g., Binney & Tremaine 1987). So, both tides and dynamical friction are efficient at erasing substructure in the inner parts. This effect is referred to as “anti-biasing” by Ghigna et al. (2000). So, on dynamical grounds, little substructure is projected within the Einstein radius. Taking the example of PG 1115+080, the projected Einstein radius is just ~ 3.6 kpc. The fraction of mass in substructure projected within a cylinder of radius ~ 3.6 kpc is clearly much lower than the global fraction of 5 per cent, which pertains to the entire dark halo of total extent ~ 200 kpc. It is crucial that lensing calculations do not assume an everywhere uniform fraction of substructure in the halo, as this does not take into account the “anti-biased” spatial distribution of substructure and therefore necessarily over-emphasises the importance of the effects of substructure on flux ratios. Notice that an interesting consequence of the spatial distribution is that anomalous flux ratios are more likely to occur for lenses with larger angular separation, as these have larger Einstein radii.

The real question at issue is the following. Suppose a simple lens model (such as a simple isothermal ellipsoid plus shear) does not adequately fit the data on positions and flux ratios. What can be legitimately deduced? The difficulty is that there are many modifications of the simple model that remove the discrepancy. One of these is substructure, as pointed out by Dalal & Kochanek and Metcalf & Zhao. As shown in this paper, another is higher order multipoles in the lensing mass, such as diskiness, boxiness, lopsidedness and barredness (see also Möller, Hewett & Blain 2003, who make a similar point). It is crucial to develop techniques to distinguish between higher order quadrupoles on the one hand and substructure on the other. From our modelling, we tend to agree that the substructure candidate B 1422+231 originally pointed out by Mao & Schneider (1998) is strong. Using a novel application of the cusp relation, Keeton, Gaudi & Petters (2002) have argued that B 2045+265 and RX J0911+0551 may be two further good candidates.

It is an outstanding problem to predict – for different cosmologies – how many quadruplets may have anomalous flux ratios. Accurate calculations will become possible only when distributions of mass and position of substructure become available from high resolution simulations. It will be interesting to see whether the numbers of lenses for which substructure is currently being claimed are compatible with cold dark matter theories.

ACKNOWLEDGMENTS

We acknowledge with gratitude the remarkable service provided to the community by the CASTLES website (C.S. Kochanek, E.E. Falco, C. Impey, J. Lehar, B. McLeod, H.-W. Rix). NWE thanks the Royal Society for financial support and HJW thanks the sub-Department of Theoretical Physics, Oxford for their hospitality during working visits. NWE acknowledges Ian Browne, Leon Koopmans and Jerry Ostriker for a number of interesting discussions. Shude Mao and Olaf Wucknitz are thanked for a helpful comments on the draft manuscript.

REFERENCES

- Agol E., Jones, B., Blaes O. 2000, ApJ, 545, 657
 Bender R., Surma P., Doebereiner S., Moellenhoff C., Madejsky R. 1989, A&A, 217, 35
 Binney J., Merrifield M. 1998, Galactic Astronomy, Princeton University Press
 Binney J., Tremaine S. 1987, Galactic Dynamics, Princeton University Press
 Bradač M., Schneider P., Steinmetz M., Lombardi M., King L.J., Porcas R. 2002, A&A, 388, 373
 Bronshtein I.N., Semendyayev K.A., 1998, Handbook of Mathematics (Springer-Verlag, New York)
 Cardone V.F., Capozziello S., Re V., Piedipalumbo E. 2002, A&A, 382, 792
 Cohn J.D. et al. 2001, ApJ, 554, 1216
 Chiba M. 2002, ApJ, 565, 17
 Christian C.A., Crabtree D., Waddell P. 1987, ApJ, 312, 45
 Colley W., Schild R.E. 2000, ApJ, 540, 104
 Crane P. et al. 1991, ApJ, 369, L59
 Dalal N., Kochanek C.S. 2002, ApJ, 572, 25
 Evans N.W. 1994, MNRAS, 267, 333
 Evans N.W., Carollo M., de Zeeuw P.T. 2000, MNRAS, 318, 1131
 Evans N.W., Hunter C. 2002, ApJ, 575, 68
 Evans N.W., Witt, H.J. 2001, MNRAS, 327, 1260
 Fabbiano G. 1989, ARAA, 27, 87
 Falco E.E., et al. 1996, AJ, 112, 897
 Falco E.E., et al. 1999, ApJ, 523, 617
 Foy R., Bonneau D., Blazit A. 1985, A&A, 149, L13
 Gerhard O.E., Kronawitter A., Saglia R.P., Bender R. 2001, AJ, 121, 1936
 Ghigna S., Moore B., Governato F., Lake G., Quinn T., Stadel J. 2000, ApJ, 544, 616
 Heyl J.S., Hernquist L., Spergel D.N. 1994, ApJ, 427, 165
 Hogg D.W., Blandford R.D. 1994, MNRAS, 268, 889
 Hunter C., Evans N.W. 2001, ApJ, 554, 1227
 Irwin M.J., Webster R.L., Hewett P.C., Corrigan R.T., Jedrzejewski R.I. 1989, AJ, 98, 1989
 Jones D.L., et al. 1996, ApJ, 470, 23
 Impey C.D., et al. 1998, ApJ, 509, 551
 Kassiola A., Kovner I. 1993, ApJ, 417, 450
 Keeton C., Gaudi B.S., Petters A.O. 2002, ApJ, submitted (astro-ph/0210318)
 Kochanek C.S. 1995, ApJ, 445, 559
 Kochanek C.S., Dalal N., astro-ph/0302036
 Kristian J. et al. 1993, AJ, 106, 1330
 Koopmans L.V.E., de Bruyn A.G. 2000, A&A, 358, 793
 Kormann R., Schneider P., Bartelmann M. 1994, A&A, 286, 357
 Kundic T., Hogg D.W., Blandford R.D., Cohen J.G., Lubin L.M., Larkin J.E. 1997, AJ, 114, 2276
 Mao S., Schneider P. 1998, MNRAS, 295, 587
 Metcalf R.B., Zhao H.S. 2002, ApJ, 567, L5
 Möller O., Hewett P.C., Blain A.W., MNRAS, in press (astro-ph/0212467)
 Moore B., Ghigna S., Governato F., Lake G., Quinn T., Stadel J., Tozzi P. 1999, ApJ, 524, L19
 Muñoz J.A., Kochanek C.S., Keeton C.R. 2001, ApJ, 558, 657
 Patnaik A.R., Browne I.W.A., Walsh D., Chaffee F.H., Foltz C.B. 1992, MNRAS, 259, 1P
 Press W.H., Flannery B.P., Teukolsky S.A., Vetterling W.T. 1999, Numerical Recipes, Cambridge University Press, Cambridge
 Rusin D., Ma C.-P. 2001, ApJ, 549, L33
 Rusin D. et al. 2002, MNRAS, 330, 205
 Saha P., Williams L.L.R. 1997, MNRAS, 292, 148
 Schechter P.L., et al. 1997, ApJ, 475, L85
 Schmidt R., Webster R.L., Lewis G.F. 1998, MNRAS, 295, 488
 Schmidt R. et al. 2002, A&A, 392, 773
 Schneider P., Ehlers J., Falco E.E., 1992, Gravitational Lenses (Springer-Verlag, New York)
 Toomre A., 1982, ApJ, 259, 535
 Trott C.M., Webster R.L. 2002, MNRAS, 334, 621
 Trotter C.S., Winn J.N., Hewitt J.N. 2000, ApJ, 535, 671
 Wambsgans J., Schneider P., Paczynski B. 1990, ApJ, 358, L33
 Winn J., Rusin D., Kochanek C. 2003, ApJ, in press (astro-ph/0212423)
 Witt H.J., Mao S. 1994, ApJ, 429, 66
 Witt H.J. 1996, ApJ, 472, L1
 Witt H.J., Mao S. 1997, MNRAS, 291, 211
 Witt H.J., Mao S. 2000, MNRAS, 311, 689
 Witt H.J., Mao S., Schechter P. 1995, ApJ, 443, 18
 Witt H.J., Mao S., Keeton, C.R. 2000, ApJ, 544, 98
 Wozniak P., et al. 2000, ApJ, 540, L65
 Wucknitz O. 2002, MNRAS, 332, 951
 Wyithe J.S.B., Agol E., Turner E.L., Schmidt R.W. 2002, MNRAS, 330, 575
 Zhao H.S., Pronk D. 2001, MNRAS, 320, 401

APPENDIX A: FULL SOLUTION BY THE VARIATION OF PARAMETERS

Observationally speaking, it is the angular structure of the density contours $G(\theta)$ that is more accessible. It is sometimes useful to be able to generate the corresponding angular structure of the lensing potential $F(\theta)$. This can be done by solving eq (2) using the method of variation of the parameters (e.g., Bronshtein & Semendyayev 1998, section 3.3.1.3.4; Evans & Witt 2001) to give

$$F(\theta) = \frac{\sin(\beta\theta)}{\beta} \left[C_1 + \int_0^\theta G(\vartheta) \cos(\beta\vartheta) d\vartheta \right] - \frac{\cos(\beta\theta)}{\beta} \left[C_2 + \int_0^\theta G(\vartheta) \sin(\beta\vartheta) d\vartheta \right]. \quad (\text{A1})$$

This establishes the relation between the potential and the surface mass density in terms of two constants C_1 and C_2 , whose values will be given shortly.

Therefore, the deflection angle has components

$$\begin{aligned} \phi_x &= r^{\beta-1} \sin(\beta-1)\theta \left[C_1 + \int_0^\theta G(\vartheta) \cos(\beta\vartheta) d\vartheta \right] \\ &\quad - r^{\beta-1} \cos(\beta-1)\theta \left[C_2 + \int_0^\theta G(\vartheta) \sin(\beta\vartheta) d\vartheta \right], \\ \phi_y &= r^{\beta-1} \cos(\beta-1)\theta \left[C_1 + \int_0^\theta G(\vartheta) \cos(\beta\vartheta) d\vartheta \right] \end{aligned}$$

$$+r^{\beta-1} \sin(\beta-1)\theta \left[C_2 + \int_0^\theta G(\vartheta) \sin(\beta\vartheta) d\vartheta \right]. \quad (\text{A2})$$

Another expression can be given for the deflection angle, namely

$$\begin{aligned} \phi_x &= \frac{\beta x}{r^{2-\beta}} F(\theta) - \frac{y}{r^{2-\beta}} F'(\theta), \\ \phi_y &= \frac{\beta y}{r^{2-\beta}} F(\theta) + \frac{x}{r^{2-\beta}} F'(\theta). \end{aligned} \quad (\text{A3})$$

By substituting the Fourier series into eqs. (A2)–(A3), we obtain expressions for the constants

$$\begin{aligned} C_1 &= \sum_k k b_k, \\ C_2 &= -\beta \frac{a_0}{2} - \sum_k \beta a_k. \end{aligned} \quad (\text{A4})$$

This completes the solution written down in eq. (A1). Given the angular structure of the density $G(\theta)$, we can find that of the potential $F(\theta)$, and vice versa.

APPENDIX B: FOURIER COEFFICIENTS OF ELLIPTICAL DISTRIBUTIONS

Let us consider the Fourier expansion of the elliptical distribution in the flat rotation curve case ($\beta = 1$)

$$F(\theta) = A(\cos^2 \theta + q^{-2} \sin^2 \theta)^{-1/2}. \quad (\text{B1})$$

The Fourier coefficients are

$$a_k = \frac{1}{\pi} \int_0^{2\pi} F(\theta) \cos(k\theta) d\theta \quad (\text{B2})$$

$$b_k = \frac{1}{\pi} \int_0^{2\pi} F(\theta) \sin(k\theta) d\theta. \quad (\text{B3})$$

However, the only non-vanishing Fourier coefficients are a_{2n} where n is an integer. The lowest-order terms are

$$\begin{aligned} a_0 &= \frac{4A}{\pi} K \\ a_2 &= \frac{4A}{\pi(1-q^2)} [(1+q^2)K - 2q^2 E] \\ a_4 &= \frac{4A}{3\pi(1-q^2)^2} [(3q^2+1)(q^2+3)K - 8q^2(1+q^2)E] \\ a_6 &= \frac{4A}{15\pi(1-q^2)^3} [(1+q^2)(15+98q^2+15q^4)K \\ &\quad - 2q^2(23+82q^2+23q^4)E] \\ a_8 &= \frac{4A}{105\pi(1-q^2)^4} [-32q^2(1+q^2)(11+74q^2+11q^4)E \\ &\quad + (105+1436q^2+3062q^4+1436q^6+105q^8)K], \end{aligned} \quad (\text{B4})$$

where K and E denote the following integrals

$$\begin{aligned} K &= \int_0^{\pi/2} \frac{d\vartheta}{(1 - (1-q^{-2}) \sin^2 \vartheta)^{1/2}} \\ E &= \int_0^{\pi/2} d\vartheta (1 - (1-q^{-2}) \sin^2 \vartheta)^{1/2}. \end{aligned} \quad (\text{B5})$$

For elliptical potential models, this gives the Fourier series for the angular function $F(\theta)$. Note that the expressions become more and more cumbersome with increasing

order. However, the Fourier series converges (numerically) extremely rapidly.

For elliptical density models, exactly the same coefficients hold good but for the Fourier expansion for $G(\theta)$, the shape function in the density. Of course, the Fourier coefficients of $G(\theta)$ are directly related to the Fourier coefficients of the potential contour $F(\theta)$ via eqs. (4) and (5).

APPENDIX C: CALCULATION OF THE ISOPHOTAL DISTORTIONS

Most giant elliptical galaxies have isophotes that are very well approximated by ellipses. The same is of course not true for disk or barred or interacting galaxies. Data from numerical simulations of halo formation are sparse, but suggest that dark haloes may also be well-approximated by ellipses (e.g., Heyl et al. 1994). So, it is useful to be able to estimate the size of the distortions of our fits from pure ellipses. This is done by computing Bender et al.'s (1989) coefficients, defined as

$$a_k^B = \frac{1}{\pi} \int_0^{2\pi} (r_i(\theta) - r_e(\theta)) \cos(k\theta), \quad (\text{C1})$$

$$b_k^B = \frac{1}{\pi} \int_0^{2\pi} (r_i(\theta) - r_e(\theta)) \sin(k\theta), \quad (\text{C2})$$

where r_i is the polar equation of the isophote and r_e is the best fitting ellipse (see also Binney & Merrifield 1998). In particular, a positive (or negative) a_4^B means that the isophotes are disk-like (or boxy).

From eqn (5), we deduce the equation of the isophote as

$$r_i = \frac{a_0}{2} + \sum_{k=2}^{\infty} [a_k(1-k^2) \cos(k\theta) + b_k(1-k^2) \sin(k\theta)]. \quad (\text{C3})$$

Here, we have specialised to the case of a flat rotation curve by setting $\beta = 1$. As shown in Section 3.3, we can transform to the coordinate system aligned with the major and minor axis and so we can set $b_2 = 0$.

Now we must determine the best fitting ellipse, which is the one which reproduces the same Fourier coefficients a_0 and a_2 as our isophote. In other words, we solve for the amplitude A and axis ratio q in eqn (B1),

$$\begin{aligned} a_0 &= \frac{4A}{\pi} K, \\ -3a_2 &= \frac{4A}{\pi(1-q^2)} [(1+q^2)K - 2q^2 E]. \end{aligned} \quad (\text{C4})$$

These equations do not have analytic solutions, but the roots can be easily obtained numerically. Having solved for A and q , our isophote r_i and the best fitting ellipse r_e have Fourier series which differ only for coefficients a_k and b_k with $k \geq 3$.

It is now straightforward to derive formulae for Bender et al.'s coefficients. Tabulated values are available in the literature only for the a_3^B and a_4^B , so we confine explicit formulae to these cases:

$$a_3^B = -8a_3, \quad (\text{C5})$$

$$a_4^B = -15a_4 - \frac{4A}{3\pi(1-q^2)^2} [(3q^2+1)(q^2+3)K - 8q^2(1+q^2)E]$$

Numerical values for the lens galaxies in Q 2237+030

PG 1115+080 are given in the main text. In both cases, the amplitudes of a_3^B and a_4^B are within the expected ranges, confirming that our solutions are realistic.

APPENDIX D: INCLUSION OF EXTERNAL SHEAR

In this appendix, we give the equations incorporating the effects of external shear. The lens equation becomes

$$\xi = x + \gamma_1 x + \gamma_2 y - \frac{\partial \phi}{\partial x}, \quad \eta = y + \gamma_2 x - \gamma_1 y - \frac{\partial \phi}{\partial y}. \quad (\text{D1})$$

The vector of observables becomes

$$\mathbf{d} = \begin{pmatrix} (1 + \gamma_1)r_\ell \cos \theta_\ell + \gamma_2 r_\ell \sin \theta_\ell, \dots, \\ (1 - \gamma_1)r_\ell \sin \theta_\ell + \gamma_2 r_\ell \cos \theta_\ell, \dots, \\ (f_{1\ell} - 1)r_1 r_\ell (1 - \gamma_1^2 - \gamma_2^2), \dots \end{pmatrix}^T, \quad (\text{D2})$$

where ℓ runs from 1 to n for a lens system with n images. The matrix C retains the same form as given in eq (22), but the coefficients $\gamma_{k\ell}$ and $\delta_{k\ell}$ become

$$\begin{aligned} \gamma_k(\theta_\ell) &= (1 - k^2)[f_{1\ell} r_\ell \cos(k\theta_1)W(\theta_1) - r_1 \cos(k\theta_\ell)W(\theta_\ell)] \\ \delta_k(\theta_\ell) &= (1 - k^2)[f_{1\ell} r_\ell \sin(k\theta_1)W(\theta_1) - r_1 \sin(k\theta_\ell)W(\theta_\ell)], \end{aligned}$$

with

$$W(\theta) = 1 + \gamma_1 \cos 2\theta + \gamma_2 \sin 2\theta. \quad (\text{D3})$$

The vector of unknowns is unchanged from eq (21). For a given external shear, the problem remains linear and can be solved by SVD.